Monthly Notices of the ROYAL ASTRONOMICAL SOCIETY

MNRAS **541,** 2393–2404 (2025) https://doi.org/10.1093/mnras/staf1101
Advance Access publication 2025 July 7

Monte Carlo radiation hydrodynamic simulations of line-driven disc winds: relaxing the isothermal approximation

Amin Mosallanezhad [1]★ Christian Knigge [1]★ Nicolas Scepi [2] James H. Matthews [3] Knox S. Long,[4,5]★ Stuart A. Sim [6] and Austen Wallis [1]

[1]*School of Physics and Astronomy, University of Southampton, Highfield, Southampton SO17 1BJ, UK*
[2]*CNRS, IPAG, Universit'e Grenoble Alpes, F-38000 Grenoble, France*
[3]*Department of Physics, Astrophysics, University of Oxford, Denys Wilkinson Building, Keble Road, Oxford OX1 3RH, UK*
[4]*Space Telescope Science Institute, 3700 San Martin Drive, Baltimore, MD 21218, USA*
[5]*Eureka Scientific Inc., 2542 Delmar Avenue, Suite 100, Oakland, CA 94602-3017, USA*
[6]*School of Mathematics and Physics, Queen's University Belfast, University Road, Belfast BT7 1NN, UK*

Accepted 2025 June 23. Received 2025 May 21; in original form 2025 April 23

ABSTRACT

Disc winds play a crucial role in many accreting astrophysical systems across all scales. In accreting white dwarfs (AWDs) and active galactic nuclei (AGNs), radiation pressure on spectral lines is a promising wind-driving mechanism. However, the efficiency of line driving is extremely sensitive to the ionization state of the flow, making it difficult to construct a reliable physical picture of these winds. Recently, we presented the first radiation-hydrodynamics simulations for AWDs that incorporated detailed, multidimensional ionization calculations via fully frequency-dependent radiative transfer, using the SIROCCO code coupled to PLUTO. These simulations produced much weaker line-driven winds ($\dot{M}_{\rm wind}/\dot{M}_{\rm acc} < 10^{-5}$ for our adopted parameters) than earlier studies using more approximate treatments of ionization and radiative transfer (which yielded $\dot{M}_{\rm wind}/\dot{M}_{\rm acc} \simeq 10^{-4}$). One remaining limitation of our work was the assumption of an isothermal outflow. Here, we relax this by adopting an ideal gas equation of state and explicitly solving for the multidimensional temperature structure of the flow. In the AWD setting, accounting for the thermal state of the wind does not change the overall conclusions drawn from the isothermal approximation. Our new simulations confirm the line-driving efficiency problem: the predicted outflows are too highly ionized, meaning they neither create optimal driving conditions nor reproduce the observed ultraviolet wind signatures. Possible solutions include wind clumping on subgrid scales, a softer-than-expected spectral energy distribution or additional driving mechanisms. With the physics now built into our simulations, we are well equipped to also explore line-driven disc winds in AGN.

Key words: accretion, accretion discs – hydrodynamics – radiative transfer – methods: numerical – novae, cataclysmic variables – stars: winds, outflows.

1 INTRODUCTION

Winds are a prominent feature of numerous astrophysical systems, particularly those involving accretion discs. Such environments, including active galactic nuclei (AGNs; e.g. Gibson et al. 2009), X-ray binaries (XRBs; e.g. Díaz Trigo & Boirin 2016; Tetarenko et al. 2018), and accreting white dwarfs (AWDs; e.g. Froning et al. 2012), frequently exhibit blueshifted absorption lines, providing clear evidence of outflowing gas. These outflows can profoundly alter the appearance of the entire system. Wind signatures observed in ultraviolet (UV) resonance lines serve as essential tools for studying outflows in astrophysical systems such as AGN. These features arise from the absorption and re-emission of UV photons by ions such as C IV, Si IV, and N V, providing insights into the velocity, ionization structure, and geometry of the winds. Moreover, the characteristic 'P Cygni' profiles and the broad absorption lines (BALs) observed in UV spectra reveal the presence of high-velocity outflows. These outflows are commonly interpreted as being driven by radiation pressure on resonance lines – a process known as 'line-driven winds'. In AGN, direct evidence for the importance of line driving comes from the 'ghost of Lyα' (e.g. Arav et al. 1995; Arav 1996; Mas-Ribas & Mauland 2019; Filbert et al. 2024) and instances of 'line locking' (e.g. Korista et al. 1993; Lu & Lin 2018) observed in the spectra of more distant luminous AGNs, such as quasi-stellar objects (QSOs), and BAL QSOs.

Beyond their observational signatures, outflows can play a crucial role as a mass, energy, and momentum sink for the underlying accretion system, while simultaneously acting as a source of these quantities for the surrounding environment. In some AWDs (Scepi, Dubus & Lesur 2019), XRBs (e.g. Ponti et al. 2012; Higginbottom et al. 2019), and ultraluminous X-ray sources (Middleton et al. 2014, 2022; Fabrika et al. 2015), a substantial fraction – if not the majority

★ E-mail: a.mosallanezhad@soton.ac.uk (AM); c.knigge@soton.ac.uk (CK); long@stsci.edu (KSL)

– of the accreted material may be ejected. Consequently, the rate of accretion onto the central object can be significantly lower than the rate at which material is supplied to the outer disc. The broader influence of outflows is perhaps most clearly illustrated by disc winds and jets driven from AGN and quasars. These outflows enable supermassive black holes to interact with their host galaxies and clusters on large scales, providing a crucial 'feedback' mechanism that shapes galaxy evolution (Silk & Rees 1998; King 2003; Fabian 2012; Morganti 2017; Harrison et al. 2018; Mosallanezhad et al. 2022).

The line-driving mechanism can significantly enhance the momentum transfer from radiation to matter, well beyond that of pure electron scattering. It was first proposed by Lucy & Solomon (1970) and subsequently developed by Castor, Abbott, & Klein (1975, hereafter CAK) to describe stellar winds from OB stars ($10^4 < T_{\rm eff,OB} < 5 \times 10^4$ K). This framework has been successfully applied to a variety of accretion disc systems, including AWDs and AGNs, where disc temperatures are comparable to those found in OB stars. In XRBs, line driving is less likely to play a dominant role since material near the compact objects tends to be very highly ionized. In these systems, thermal and/or magnetic driving may be responsible for the observed outflows (Miller et al. 2016; Higginbottom et al. 2017; Tomaru et al. 2020).[1]

In principle, radiation-driven winds will be generated in the vicinity of luminous sources whenever the outward force imparted via photon scattering and/or absorption exceeds the inward gravitational pull; the well-known Eddington limit (Eddington 1916) corresponds to the simplest scenario in which the radiative force arises purely via electron scattering, with $L_{\rm Edd}$ representing the threshold luminosity above which radiation pressure overcomes gravity. Extending this concept, line driving takes place in media that are not fully ionized, allowing photons to interact with bound electrons. These additional interactions can greatly amplify the overall radiative thrust. The factor by which the radiative force surpasses its value in an electron-only scattering regime is termed the force multiplier, $\mathcal{M}$, a designation first introduced by CAK. Under optimal ionization conditions, this multiplier can be as large as $\mathcal{M} \simeq$ a few $\times\, 10^3$ (Gayley 1995; Proga, Stone & Drew 1998; Higginbottom et al. 2024).

Numerical simulations of line-driven disc winds have been conducted both in systems hosting AWDs (Pereyra, Kallman & Blondin 1997, 2000; Proga et al. 1998; Dyda & Proga 2018a, b) and in the context of AGN-scale systems (Proga, Stone & Kallman 2000; Proga & Kallman 2004; Liu et al. 2013; Nomura et al. 2016; Nomura & Ohsuga 2017; Mosallanezhad et al. 2019; Nomura, Ohsuga & Done 2020; Dyda, Davis & Proga 2024; Dyda et al. 2025). A key element in such simulations is determining how the force multiplier is distributed throughout the outflowing material. More precisely, the force multiplier directly depends on the ionization state, ξ, of the wind, which, in turn, is governed by radiative processes. At the same time, the radiation field itself is altered by its interactions with the outflowing gas. Consequently, matter and radiation are intricately coupled, each influencing the other in non-linear, complex ways within these line-driven outflows.

Previous simulations have significantly simplified this complex interplay by employing the standard CAK $k-\alpha$ parametrization, $\mathcal{M} = k\, t^{-\alpha}$. In this formulation, t is the so-called optical depth parameter, which depends on local velocity gradients, while the exponent α captures the relative importance of optically thin versus optically thick lines. Finally, k acts as a normalization factor that represents the overall effectiveness of line driving. In their AWD simulations, Proga et al. (1998) adopted $k = 0.2$ and $\alpha = 0.6$, guided by typical wind parameters in OB stars (Gayley 1995). For their AGN models, Proga et al. (2000) likewise used $\alpha = 0.6$, but replaced the constant k with a function, $k(\xi)$, derived from the work of Stevens & Kallman (1990). They also typically set the maximum allowed force multiplier to $\mathcal{M}_{\rm max} \approx 4400$.

Despite early simulations successfully producing line-driven winds with mass-loss rates of $\dot{M}_{\rm wind} \sim 10^{-4}\dot{M}_{\rm acc}$ (Proga et al. 1998, 1999), certain discrepancies emerged (Drew & Proga 2000; Proga et al. 2002). For instance, reproducing the strengths of wind-formed spectral lines in AWD systems required accretion rates that were higher than expected by a factor of 2–3. This hinted that some underlying assumptions may not be entirely accurate, although Proga (2003) found that theory and observations might be consistent after all. Later, more detailed radiative transfer calculations (Sim et al. 2010; Higginbottom et al. 2014) revealed that multidimensional scattering effects in AGN outflows caused the winds to become overionized, disrupting effective line driving. These findings highlight a key concern: the force multipliers and ionization states assumed in these simulations – based on the near-optimal conditions found in OB stars – may not accurately reflect real astrophysical environments.

To overcome these challenges, we (Higginbottom et al. 2024) presented the first Monte Carlo radiation-hydrodynamics (MC-RHD) simulations, utilizing the PLUTO hydrodynamics code coupled with the SIROCCO radiative transfer code. These simulations incorporated detailed, multidimensional ionization state calculations via fully frequency-dependent radiative transfer, while self-consistently treating radiation transport and force multipliers in a unified framework. We focused on AWD systems because of their limited spatial dynamic range and simpler spectral energy distribution (SED) made them more manageable compared to AGN. In these simulations, we assumed an isothermal outflow at a constant temperature of $T = 40\,000$ K. Our main finding was that the physical conditions in AWD environments were far less conducive to efficient line driving than previously assumed. Unlike the conditions found in hot, single-star winds, the ionization states in these systems turned out to be significantly higher. Since these sources are only marginally luminous enough to sustain strong line-driven flows, this overestimation had profound implications. We found that the mass-loss rates were lower by approximately two orders of magnitude compared to previous estimates. Similarly, the synthetic spectra produced in our simulations did not match observational data. These results collectively raised serious questions about the viability of line driving as the primary mechanism responsible for the winds observed in AWDs.

In our previous simulations, we assumed that the outflow was isothermal, a significant simplification that ignores the temperature-dependent aspects of ionization balance and radiative cooling/heating processes that govern the efficiency of line-driven winds. For modelling winds in AGN, which is our ultimate goal and where the SEDs are inherently more complex and harder to parametrize than those of AWDs, the isothermal approximation becomes particularly problematic. To address this, we replace the isothermal assumption with an ideal gas equation of state and directly solve the full set of energy equations. This enables us to resolve the spatial temperature structure of the outflow, driven by radiative and hydrodynamic heating/cooling processes. Critically, we also track the evolving SED within the outflow as it is locally attenuated, a feature essential for

[1]Recent observations of optical (e.g. Mata Sánchez et al. 2018; Muñoz-Darias et al. 2019) and UV (e.g. Castro Segura et al. 2022) wind signatures in XRBs reveal lower ionization material, implying that line driving may contribute to mass ejection in some of these systems.

AGN applications where overionization can suppress line driving. Our approach integrates these advancements with an enhanced 'macro-atom' method for radiative transfer (Lucy 2002, 2003), which more rigorously enforces energy conservation in the comoving frame and results in a more accurate treatment of the reprocessing effect of the wind.

The remainder of this paper is organized as follows. In Section 2, we begin with a brief overview of our previous simulations and then detail the newly developed methods used to perform 2.5D, multifrequency radiation-hydrodynamics (RHD) simulations with an ideal gas equation of state. This approach includes a full treatment of ionization, line-driving forces, and radiative heating/cooling rates. In Section 3, we present the results of our simulations, some of which are directly compared against those from our previous isothermal models. Finally, in Section 4, we discuss our findings, examine the limitations of our calculations, and summarize our conclusions.

2 METHODS

2.1 Hydrodynamics incorporating radiative heating/cooling, and acceleration

Our MC-RHD simulations employ the publicly available Godunov-type hydrodynamics code PLUTO (v4.4; Mignone et al. 2007), coupled with the Monte Carlo radiative transfer code SIROCCO (Long & Knigge 2002; extended by Sim, Drew & Long 2005; Higginbottom et al. 2013; Matthews et al. 2015, 2025). The two codes are integrated via an operator-splitting formalism, in which SIROCCO supplies heating and cooling rates, as well as radiative accelerations. Our methodology is based on that described by Higginbottom et al. (2024), with the key difference being the explicit inclusion of the ideal gas equation of state and the solution of the full energy equation.

Allowing for radiative forces, the hydrodynamic continuity and momentum equations can be written as

$$\frac{\partial \rho}{\partial t} + \nabla \cdot (\rho \boldsymbol{v}) = 0, \tag{1}$$

$$\frac{\partial (\rho \boldsymbol{v})}{\partial t} + \nabla \cdot (\rho \boldsymbol{v}\boldsymbol{v} + p\mathbf{I}) = -\rho \nabla \Phi + \rho \boldsymbol{g}_{\rm rad}. \tag{2}$$

Here ρ is the gas density, $\boldsymbol{v}$ is the velocity vector, p is the gas pressure, $\mathbf{I}$ is the identity matrix, Φ is the gravitational potential, and $\boldsymbol{g}_{\rm rad}$ represents the radiative acceleration.

In our previous simulations, we assumed the outflow to be isothermal, so these equations were supplemented with

$$p = \rho c_{\rm iso}^2, \tag{3}$$

i.e. the isothermal equation of state. We adopted a fixed sound speed $c_{\rm iso} = 24\,{\rm km\,s^{-1}}$, corresponding to a fixed temperature of $T = 40\,000\,{\rm K}$. With these assumptions, there was no need to solve the full energy equation.

In our new simulations, we relax the isothermal assumption and instead adopt the ideal gas equation of state:

$$p = n k_{\rm B} T, \tag{:4}$$

where n is the total particle number density, and $k_{\rm B}$ is the Boltzmann constant. We then need to solve the full energy equation, which can be written as

$$\frac{\partial E}{\partial t} + \nabla \cdot [(E + p)\boldsymbol{v}] = -\rho \boldsymbol{v} \cdot \nabla \Phi + \rho \boldsymbol{v} \cdot \boldsymbol{g}_{\rm rad} + \rho \mathcal{L}. \tag{5}$$

Here, $E = (1/2)\rho|\boldsymbol{v}|^2 + \rho e$ represents the total gas energy density, where e is the internal energy per unit mass, and $\mathcal{L}$ is the net radiative heating/cooling rate per unit mass. We neglect relativistic effects and adopt a Newtonian gravitational potential, $\Phi = -GM_{\rm WD}/r$, where $M_{\rm WD}$ is the mass of the white dwarf, and G is the gravitational constant. For a monatomic ideal gas, the internal energy per unit mass, e, is related to the pressure and density by $e = p/[\rho(\gamma - 1)]$, where $\gamma = 5/3$ is the adiabatic index.

In our simulations, PLUTO is responsible for solving and advancing this coupled system of equations, with SIROCCO providing updates for two critical terms: the radiative acceleration $\boldsymbol{g}_{\rm rad}$ and the net radiative heating/cooling rate $\mathcal{L}$. Because the radiative transfer is much more expensive computationally than the hydrodynamical portion of the calculation, we carry out radiative transfer and ionization calculations at intervals significantly longer than the hydrodynamic time-step, specifically at $\Delta t_{\rm RAD} \gg \Delta t_{\rm HD}$. Typically, we set $\Delta t_{\rm RAD} = 2\,{\rm s}$, which corresponds to about $10^3\,\Delta t_{\rm HD}$ in our simulations. For this to be a reasonable approach, the ionization state and radiation field within each cell remain approximately constant over the time-scale $t_{\rm RAD}$. We have verified that our results are not sensitive to the exact value of $\Delta t_{\rm RAD}$ within this regime.[2] Next, we cycle between hydrodynamic and radiative updates until the entire wind structure evolves to a quasi-steady state.[3]

In order to avoid abrupt temperature changes every $\Delta t_{\rm RAD}$ (when exact new radiative heating/cooling rates become available), we apply approximate updates to $\mathcal{L}$ at each hydrodynamic time-step. These approximate updates are based on the estimated impact of the changing temperature and density on the radiative heating/cooling rates. We also apply a damping factor when we update $\mathcal{L}$ after each call to SIROCCO. The way in which we calculate and update radiative heating and cooling rates is described in more detail in Section 2.5.

Similarly, the radiative acceleration $\boldsymbol{g}_{\rm rad}$ is updated approximately at each hydrodynamic time-step. Here, the approximate updates account for changes in the velocity field, while assuming that the ionization state of the flow stays approximately constant over a time-scale $\Delta t_{\rm RAD}$. The way in which we calculate and update $\boldsymbol{g}_{\rm rad}$ is described in more detail in Section 2.3.

2.2 Ionization and radiative transfer

After each simulation time interval of $\Delta t_{\rm RAD}$, SIROCCO is activated and loads the latest snapshots of the density, velocity fields, and temperature calculated by PLUTO, as well as the wind's ionization state from its previous run. Photon packets are then introduced into the outflow by both the accretion disc and the wind. These packets are tracked as they journey through the wind, where they may undergo attenuation due to bound–free and free–free opacity, electron scattering, and bound–bound interactions. The photon packets passing through each cell are used to build estimators that represent the radiation field within that cell. This information is then used to update

[2]We performed a simulation test using $\Delta t_{\rm RAD} = 0.2\,{\rm s}$ and find that the wind mass-loss rate deviates by less than 5 per cent from $\Delta t_{\rm RAD} = 2.0\,{\rm s}$ model, while the ionization structure shows only marginal variations at high latitudes. These results confirm that adopting $\Delta t_{\rm RAD} = 1000\,\Delta t_{\rm HD}$ captures the essential dynamics without significant loss of accuracy – consistent with Higginbottom et al. (2024) – and demonstrate that our conclusions are insensitive to the precise choice of $\Delta t_{\rm RAD}$ within this regime.

[3]By 'quasi-steady', we mean a flow in which the mass-loss rate and overall geometry are no longer changing systematically with time. As previously found in RHD simulations of line-driven winds, the smaller scale outflow structure is inherently time variable, even once this quasi-steady state is reached (Proga et al. 1998, 1999; Higginbottom et al. 2024).

the wind's ionization state and to calculate the radiative accelerations and radiative cooling/heating rates.

We begin by assuming that the disc initially has an effective temperature distribution following the standard Shakura & Sunyaev (1973) model

$$T_{\rm d,\,visc}(R) = T_* \left(\frac{R_{\rm WD}}{R}\right)^{3/4} \left(1 - \frac{R_{\rm WD}}{R}\right)^{1/4}, \tag{6}$$

where $R = r \sin\theta$ denotes the cylindrical radius, and

$$T_* = \left(\frac{3GM_{\rm WD}\dot{M}_{\rm acc}}{8\sigma\pi R_{\rm WD}^3}\right)^{1/4}. \tag{7}$$

Here, $\dot{M}_{\rm acc}$ represents the accretion rate through the disc, and σ is the Stefan–Boltzmann constant. For the purpose of generating photon packets, the disc is divided into concentric annuli, each initially considered to radiate as a blackbody with an effective temperature given by $T_{\rm d,\,eff} = T_{\rm d,\,visc}(R)$. This set-up determines both the number and the frequency distribution of the photon packets produced by each annulus. To be more precise, the plasma within the simulation domain itself generates photons through free–free, free–bound, and bound–bound processes.

As photons traverse the wind, they are employed to update three sets of estimators related to the radiation field: (i) the angle-averaged mean intensity J_ν, (ii) the direction-dependent UV flux $F_{{\rm UV},i}$, and (iii) the radiative cooling and heating terms. Here, the index i denotes one of $N_{\hat{n}} = 36$ directions chosen to effectively sample all possible vectors in the $\phi = 0$ plane. The UV band is defined to span frequencies from 7.4×10^{14} to 3×10^{16} Hz. The flux estimator $\boldsymbol{F}_{{\rm UV},i}$ is utilized by PLUTO to compute the radiative accelerations (see Section 2.3), while the mean intensity estimator J_ν is used to determine the ionization state of the gas and the corresponding relationship between the force multiplier and the optical depth parameter (refer to Section 2.4). Additionally, the radiative cooling and heating terms are passed to PLUTO to calculate the total cooling rate (see Section 2.5 for more details).

After the photon transport phase is complete, SIROCCO calculates the ionization state of the gas based on the local density, temperature, and the frequency-dependent intensity J_ν. The estimator for J_ν inherently accounts for any attenuation of photon packets within the wind, as well as re-emission from the wind itself. Critically, it also includes photons that arrive in a cell from other regions of the wind, including those introduced via scattering events. This scattered and/or reprocessed component of the radiation field makes it much harder for material close to the centre (e.g. a failed wind) to effectively shield material located further out.

Whenever SIROCCO is called, we execute at least two iterations encompassing the entire process of photon generation, radiation transport, ionization equilibrium calculations, and evaluation of the radiative cooling and heating terms. This iterative method enables us to account for the effects of irradiation on the temperature distribution of the disc. Some photon packets emitted by the central source and some that have been reprocessed in the outflow will unavoidably impact the disc's surface. In SIROCCO, these photons can be managed in one of three ways: (i) by discarding them; (ii) by assuming they are absorbed and reprocessed; or (iii) by treating them as specularly reflected. In the simulations presented here, we choose option (ii). Consequently, after the first iteration, we update the effective temperature distribution across the disc such that

$$\sigma T_{\rm d,\,eff}^4(R) = \sigma T_{\rm d,visc}^4(R) + F_{\rm irr}(R), \tag{8}$$

where $F_{\rm irr}(R)$ is the irradiating flux incident on the disc at radius R.

2.3 Radiative acceleration

The net radiative acceleration in each cell, $\boldsymbol{g}_{\rm rad}$, is computed as a vector sum over $N_{\hat{n}}$ directions uniformly distributed in the $\phi = 0$ plane, ensuring equal angular spacing between each direction,

$$\boldsymbol{g}_{\rm rad} = \sum_{i=1}^{N_{\hat{n}}} g_i = \sum_{i=1}^{N_{\hat{n}}} [1 + \mathcal{M}(t_i)]\,\sigma_{\rm e}\frac{\boldsymbol{F}_{{\rm UV},i}}{c}. \tag{9}$$

Here, $\sigma_{\rm e}$ is the Thompson cross-section per unit mass, c is the light speed, and g_i and $\boldsymbol{F}_{{\rm UV},i}$ represent the radiative acceleration and UV flux in direction i, respectively. We conducted our simulations with a directional resolution of $N_{\hat{n}} = 36$. Tests at a higher resolution ($N_{\hat{n}} = 72$) showed no significant differences in the final results; the character of the wind remained nearly identical, with mass-loss rates differing by less than 1 per cent between the two simulations.

In equation (9), $\mathcal{M}(t_i)$ represents the force multiplier, which parametrizes the effective number of lines available to enhance the scattering coefficient. This quantity varies based on the ionization level of the material within each cell (see Section 2.4). Notably, the force multiplier depends on the optical depth parameter t_i, defined as

$$t_i = \sigma_{\rm e}\rho v_{\rm th}\left|\frac{{\rm d}(\boldsymbol{v}\cdot\hat{n}_i)}{{\rm d}s_i}\right|^{-1}, \tag{10}$$

where $v_{\rm th} = \sqrt{2k_{\rm B}T/m_{\rm p}}$ is the thermal velocity of the gas, ${\rm d}s_i$ represents an infinitesimal step along the direction $\hat{n}_i$, and $|{\rm d}(\boldsymbol{v}\cdot\hat{n}_i)/{\rm d}s_i|$ is the gradient of the velocity component projected in this direction. Therefore, in this study, by adopting an ideal gas equation of state, $\mathcal{M}(t_i)$ becomes direction-dependent and is sensitive to the instantaneous local velocity field as well as the temperature distribution. It is worth highlighting that even though the ionization state of the flow is updated only every $\Delta t_{\rm RAD}$, the optical depth parameter – and hence the force multiplier – is adjusted continuously (at each hydrodynamic time-step) to account for the changing velocity field in each cell.

These conceptually simple expressions capture the complex non-linear coupling between matter and radiation in line-driven flows. The radiation field and ionization state depend on the outflow dynamics – which in turn control the density, velocity fields, and temperature. Conversely, the dynamics are influenced by the radiation field and ionization state, which affect $F_{{\rm UV},i}$, $\mathcal{M}(t_i)$, and the net radiative rate.

2.4 Generating a lookup table for the force multiplier

We follow Higginbottom et al. (2024) in utilizing the approach described by Parkin & Sim (2013) to generate updated lookup tables for the local force multiplier, considering the SED and ionization parameter within each cell. We do not employ SIROCCO directly for this task because calculating precise force multipliers requires a more extensive line list than the one SIROCCO uses. SIROCCO's line list is sufficient for obtaining the accurate estimate of J_ν needed to determine the ionization state, but not for the detailed force multiplier calculations. Essentially, we provide the ionization state and the local estimate of J_ν to an independent code that has access to over 450 000 spectral lines (see Parkin & Sim 2013 for further details). For each transition, the code begins by calculating the quantity

$$\eta_{\rm u,l} = \frac{hc}{4\pi}\frac{n_{\rm l}B_{\rm l,u} - n_{\rm u}B_{\rm u,l}}{\sigma_{\rm e}\rho v_{\rm th}}, \tag{11}$$

where u and l refer to the upper and lower levels of the relevant transition, respectively. Here, $n_{\rm u}$ and $n_{\rm l}$ are the upper and lower level number densities of ions supplied by SIROCCO, and $B_{\rm l,u}$ and $B_{\rm u,l}$ are the usual Einstein coefficients for absorption and stimulated

emission, respectively. The force multiplier $\mathcal{M}(t)$ is determined as a weighted sum of contributions from all line transitions:

$$\mathcal{M}(t) = \sum_{\text{lines}} \Delta\nu_{\text{D}} \frac{J_\nu}{J} \frac{1 - \exp(-\eta_{\text{u,l}}\, t)}{t}, \tag{12}$$

where $\Delta\nu_{\text{D}} = \nu_0 v_{\text{th}}/c$ represents the Doppler width of each line with ν_0 as the central frequency of the line.

2.5 Heating and cooling rates

After each call to SIROCCO, i.e. every Δt_{RAD}, we pass updated radiative heating and cooling rates back to PLUTO. However, as already noted in Section 2.1, we do not take the radiative heating and cooling rates to be constant between these calls. Instead, we apply approximate updates to these rates at each hydrodynamic time-step in order to allow for rapid changes in the local density, temperature, and ionization state. These approximate updates are essentially a way to interpolate the radiative heating and cooling rates across Δt_{RAD}. The purpose of this technique is to facilitate convergence by preventing unphysically abrupt changes in the simulation after calls to SIROCCO.

In practice, we calculate approximate updates to $\rho\mathcal{L}$ at each hydrodynamic time-step by using slightly modified versions of the analytic heating and cooling rate equations given by Higginbottom et al. (2018) (which are themselves based on Blondin 1994; also see Higginbottom & Proga 2015; Higginbottom et al. 2017). In these equations, the net radiative heating and cooling rate is broken up into five heating and cooling terms: Compton heating (H_{c}) and Compton cooling (Λ_{c}), X-ray (photoionization+Auger) heating rate (H_{x}), bremsstrahlung cooling (Λ_{b}), and cooling via line emission (Λ_{l}). All five heating and cooling rates are then combined to give an estimate of the total net rate

$$\rho\mathcal{L} = n_{\text{H}} \left(n_{\text{e}} H_{\text{c}} + n_{\text{H}} H_{\text{x}} - n_{\text{e}} \Lambda_{\text{c}} - n_{\text{e}} \Lambda_{\text{b}} - n_{\text{e}} \Lambda_{\text{l}} \right), \tag{13}$$

where n_{H} and n_{e} are the number densities of hydrogen and electrons, respectively. Following Higginbottom et al. (2018), we approximate the electron-to-hydrogen density ratio as

$$\frac{n_{\text{e}}}{n_{\text{H}}} = \begin{cases} 2.5 \times 10^{-52}\, T^{12.3}, & T < 1.5 \times 10^4\,\text{K}, \\ 2.5 \times 10^{-3.8}\, T^{0.86}, & 1.5 \times 10^4 \leq T < 3.3 \times 10^4\,\text{K}, \\ 1.21, & T \geq 3.3 \times 10^4\,\text{K}. \end{cases} \tag{14}$$

The heating and cooling terms can then be expressed as

$$H_{\text{c}} = K_{H_{\text{c}}} \left[8.9 \times 10^{-36}\, \xi\, T_{\text{x}} \right] \ (\text{erg s}^{-1}\,\text{cm}^3), \tag{15}$$

$$\Lambda_{\text{c}} = K_{\Lambda_{\text{c}}} \left[8.9 \times 10^{-36}\, \xi\, (4T) \right] \ (\text{erg s}^{-1}\,\text{cm}^3), \tag{16}$$

$$H_{\text{x}} = K_{H_{\text{x}}} \left[1.5 \times 10^{-21}\, \xi^{1/4} T^{-1/2} \right] \ (\text{erg s}^{-1}\,\text{cm}^3), \tag{17}$$

$$\Lambda_{\text{b}} = K_{\Lambda_{\text{b}}} \left[3.3 \times 10^{-27}\, T^{1/2} \right] \ (\text{erg s}^{-1}\,\text{cm}^3) \tag{18}$$

$$\Lambda_{\text{l}} = K_{\Lambda_{\text{l}}} \left[1.0 \times 10^{-16}\, \frac{\exp\left(-1.3 \times 10^5/T\right)}{T\sqrt{\xi}} + \mathcal{K}(T) \right] \times (\text{erg s}^{-1}\,\text{cm}^3), \tag{19}$$

where

$$\mathcal{K}(T) = \begin{cases} 5.0 \times 10^{-27} T^{1/2}, & T < 10^4\,\text{K}, \\ 1.0 \times 10^{-24}, & 10^4 < T < 10^7\,\text{K}, \\ 1.5 \times 10^{-17} T^{-1}, & T > 10^7\,\text{K}. \end{cases} \tag{20}$$

The quantity $\xi \left[= 4\pi F_{\text{ion}} n_{\text{H}}^{-1} \right]$ in these equations is the so-called ionization parameter (where F_{ion} denotes the hydrogen-ionizing flux).

These analytic expressions – without the 'K prefactors' – were originally designed to approximate the heating and cooling rates for material irradiated by a bremsstrahlung SED. However, the scalings of the terms with temperature, density, and ionization parameter should be fairly robust to SED changes, and it is only these scalings that our approximate updating method actually relies on.

Specifically, the analytic expressions are implemented in PLUTO and used to continually update the radiative heating and cooling rates at each hydrodynamic time-step. However, they are recalibrated after each call to SIROCCO by adjusting the K prefactors so that the approximate rates match the *actual* rates (as calculated by SIROCCO).

To prevent abrupt changes in the heating and cooling rates, we apply a numerical damping factor during the recalibration process after each ionization and radiative transfer (IRT) step. While the simulation is expected – and observed – to converge to a quasi-steady state, the exact trajectory to this state is not critical. The numerical damping facilitates convergence without impacting the final results. We have tested this approach by using various damping factors and confirmed its robustness. For our final runs, we used a damping factor of 0.9, meaning the calibration factors can change by no more than 10 per cent after each IRT step.

2.6 System parameters and computational set-up

The system parameters and numerical set-up we adopt largely follow those used for Model HK22D by Higginbottom et al. (2024), which they used as their fiducial reference model. However, we summarize the key points here briefly for completeness. Our numerical grid is set up in spherical polar coordinates (r, θ, ϕ). The computational domain is defined in two dimensions, spanning $r_{\text{min}} \leq r \leq r_{\text{max}}$ and $0 \leq \theta \leq \pi/2$, covering one quadrant of the environment near the white dwarf for hydrodynamical calculations. We set $r_{\text{min}} = r_{\text{WD}}$ and $r_{\text{max}} = 10\, r_{\text{WD}}$, where r_{WD} is the radius of the white dwarf.[4] The parameters are fixed as $M_{\text{WD}} = 0.6\,\text{M}_\odot$ and $r_{\text{WD}} = 8.7 \times 10^8$ cm.

The r–θ plane is divided into zones as follows: in the r-direction, the domain is discretized into 128 zones with a geometric progression such that $\text{d}r_i/\text{d}r_{i+1} = 1.05$. Similarly, in the θ-direction, the domain consists of 96 zones with $\text{d}\theta_j/\text{d}\theta_{j+1} = 0.95$. This spacing ensures the highest resolution in the wind-launching region, particularly near the accretor and the disc plane. The only 'net' radiation source in our model is the accretion disc: there is no central source, and the wind only reprocesses disc photons. As discussed and shown by Higginbottom et al. (2024), this is the most optimistic assumption for successful line driving. The accretion rate is set to $\dot{M}_{\text{acc}} = \pi \times 10^{-8}\,\text{M}_\odot\,\text{yr}^{-1}$, which is at the high end of the typical range for wind-driven accretion-disc systems, such as nova-like variables (Howell & Mason 2018).

We assume a disc that is geometrically thin [Shakura–Sunyaev disc (SSD); Shakura & Sunyaev 1973], meaning all the radiation from the disc originates from the system's mid-plane at $\theta = \pi/2$. Since the disc serves as the mass reservoir for the outflow, we set the density at mid-plane to a fixed value and maintain this constant throughout

[4]Our primary goal here is to compare our ideal equation of state and macro-atom mode simulations with the isothermal wind models of Higginbottom et al. (2024), which were computed over a radial domain of $10\, r_{\text{WD}}$. To assess the impact of domain size, we performed a test run extending the outer boundary to $r_{\text{max}} = 50\, r_{\text{WD}}$ and adopting the mid-plane density of $\rho(r, \theta = \pi/2) \propto r^{-\alpha}$ with $\alpha = 0.5$. The simulation reaches a steady state after approximately 400 s, and the average mass-loss rate matches that of our fiducial model closely, confirming that extending the radial domain does not significantly alter the global wind properties.

Table 1. Parameters adopted in the simulations and some derived quantities. For each simulation, we provide the model designation (column 'name'), its SIROCCO mode, the equation of state, the equivalent models in HK, the accretion rate ($\dot{M}_{\rm acc}$), the wind mass-loss rate ($\dot{M}_{\rm wind}$), and the velocity of the fast parts of the wind ($v_{\rm r}$). Full parameter files are available in the code repository (see Data Availability section).

Name	SIROCCO mode	Equation of state	Wind temperature (K)	Eqv. model in HK24	$\dot{M}_{\rm acc}$ ($M_\odot\,{\rm yr}^{-1}$)	$\dot{M}_{\rm wind}$ ($M_\odot\,{\rm yr}^{-1}$)	$v_{\rm r}$ (km s^{-1})
(1)	(2)	(3)	(4)	(5)	(6)	(7)	(8)
Model A	Hybrid macro-atom	Ideal	Variable	...	$\pi \times 10^{-8}$	6.3×10^{-14}	1900
Model B	Hybrid macro-atom	Isothermal	40 000	...	$\pi \times 10^{-8}$	5.6×10^{-14}	1250
Model C	Classic	Ideal	Variable	...	$\pi \times 10^{-8}$	3.6×10^{-14}	1700
Model D	Classic	Isothermal	40 000	HK22D	$\pi \times 10^{-8}$	4.6×10^{-14}	1700

Note. Here, HK24 refers to our previous simulations, i.e. Higginbottom et al. (2024).

the simulations. Ideally, this density, $\rho_{\rm d}$, should correspond to the upper regions of the disc's atmosphere, just below where the wind is launched. For our simulations, $\rho_{\rm d}$ must be set sufficiently high to ensure that the critical and sonic points of the outflow fall within the simulation domain, but not so high that the hydrostatic regions within the domain become optically thick. We typically choose $\rho_{\rm d} = 10^{-9}\,{\rm g\,cm^{-3}}$ to achieve this balance. We tested variations in $\rho_{\rm d}$ by factors of 2 and according to the standard SSD model, finding no significant changes in the wind solution; the global wind properties remain robust. Therefore, as long as $\rho_{\rm d}$ is chosen to correctly capture the sonic point, while avoiding excessive optical thickness at the base of the wind, our results remain relatively insensitive to its precise value. The initial density distribution across the grid is determined through hydrostatic equilibrium in the latitudinal direction, expressed as

$$\rho(r,\theta) = \rho_{\rm d} \exp\left(-\frac{GM_{\rm WD}}{2c_{\rm s}^2 r \tan^2\theta}\right). \tag{21}$$

Here, $c_{\rm s} = \sqrt{\gamma k_{\rm B} T/(\mu m_{\rm p})}$ is the sound speed, and $\mu = 0.6$ and $m_{\rm p}$ are the mean molecular weight and proton mass, respectively. The initial temperature distribution is set via equation (6), i.e. $T(r,\theta) = T_{\rm d,visc}$. The initial pressure is given by $p = \rho c_{\rm s}^2/\gamma$. For the initial velocity, we assume $v_{\rm r} = v_\theta = 0$, and $v_\phi = v_{\rm k}$, where $v_{\rm k}$ is the Keplerian velocity. For isothermal simulations, we fix the temperature to $T = 40\,000\,{\rm K}$, which corresponds to an isothermal sound speed of $c_{\rm iso} = 24\,{\rm km\,s^{-1}}$.

In all of our simulations, we impose a density floor of $\rho_{\rm floor} = 10^{-24}\,{\rm g\,cm^{-3}}$. If the density in a cell falls below this threshold, it is reset to $\rho_{\rm floor}$ while conserving both momentum and energy.

After each hydrodynamic time-step, $\Delta t_{\rm HD}$, the mid-plane temperatures and densities are reset to $T_{\rm d,\,visc}$ and $\rho_{\rm d}$ to $10^{-9}\,{\rm g\,cm^{-3}}$, respectively. After resetting the mid-plane density, we also update the velocity in the θ direction v_θ, to ensure momentum conservation in this direction.

We adopt outflow boundary conditions at the innermost and outermost radial cells. The boundary at $\theta = 0$ is treated as axisymmetric, while reflection symmetry is assumed at the mid-plane, $\theta = \pi/2$. For all of our simulations, we employ PLUTO's standard hydrodynamics module with linear reconstruction. Time integration is performed using a second-order Runge–Kutta scheme, with a Courant–Friedrichs–Lewy number of 0.4. We adopt the Harten–Lax–van Leer approximate Riemann solver, which is robust in handling discontinuities.

To initialize the radiative force, we use SIROCCO to compute the ionization state, direction-dependent fluxes, and radiative cooling/heating terms following the procedure outlined in Sections 2.1–2.5. This allows us to initialize the radiation force and radiative cooling/heating in PLUTO for the first time-step. Each time SIROCCO is called – i.e. after each $\Delta t_{\rm RAD}$ – we run two 'ionization cycles' (cf. Matthews et al. 2025), each of which tracks 10^7 energy packets through the computational domain. All simulations were evolved for a total of 1500 s, at which point they had all reached quasi-steady states.

As discussed by Matthews et al. (2025), SIROCCO offers two modes of operation for radiative transfer: the hybrid macro-atom mode, which is generally more physically accurate, and the classic mode. In the latter, Monte Carlo packets are allowed to lose energy due to continuum opacity as they traverse the flow, with this energy taken up by packets emitted separately by the wind. In the former, near radiative equilibrium and comoving frame energy conservation are instead enforced rigorously at the point of interaction. In addition, the hybrid macro-atom mode makes use of the macro-atom formalism (Lucy 2002, 2003), in our case treating both H and He as macro-atoms and the remaining metals as 'simple atoms' within a two-level approximation for line transfer (see Matthews et al. 2025, section 3, for more details). One beneficial aspect of this approach is that the bound–free continua of H and He ions, as well as their recombination cascades, are treated more accurately. In our previous RHD simulations, we only employed the classic mode. We now run each of our isothermal and ideal gas simulations using both radiative transfer modes, which allows us to test if any of our science conclusions are sensitive to the details of the methods. It also acts as a proof-of-concept, since this is, to our knowledge, the first time an RHD simulation of line-driven winds has used a version of the macro-atom formalism.

3 RESULTS

We performed four simulations to investigate the impact of the ideal versus isothermal equations of state while employing the two different SIROCCO modes described above: the hybrid macro-atom and the classic modes. The detailed parameters for these models are listed in columns (1)–(6) of Table 1. Specifically, Models A and B utilize the SIROCCO hybrid macro-atom mode to directly compare the behaviour of the ideal and isothermal cases, whereas Models C and D are executed using the classic SIROCCO mode. Model D in our simulations is identical in set-up to Model HK22D from Higginbottom et al. (2024). The key parameters describing our simulations are summarized in Table 1. Model A represents our most physically complete simulation of a line-driven accretion disc wind to date.

Fig. 1 displays a snapshot of the density distribution, overlaid with the poloidal velocity $v_{\rm p} = (v_{\rm r}^2 + v_\theta^2)^{1/2}$, for our fiducial model. This plot corresponds to $t = 850\,{\rm s}$ of simulation time, approximately one-fifth of the sound-crossing time-scale, at which point the simulation has reached a quasi-steady state. In this figure, the colour map represents the logarithmic density, while the overlaid velocity

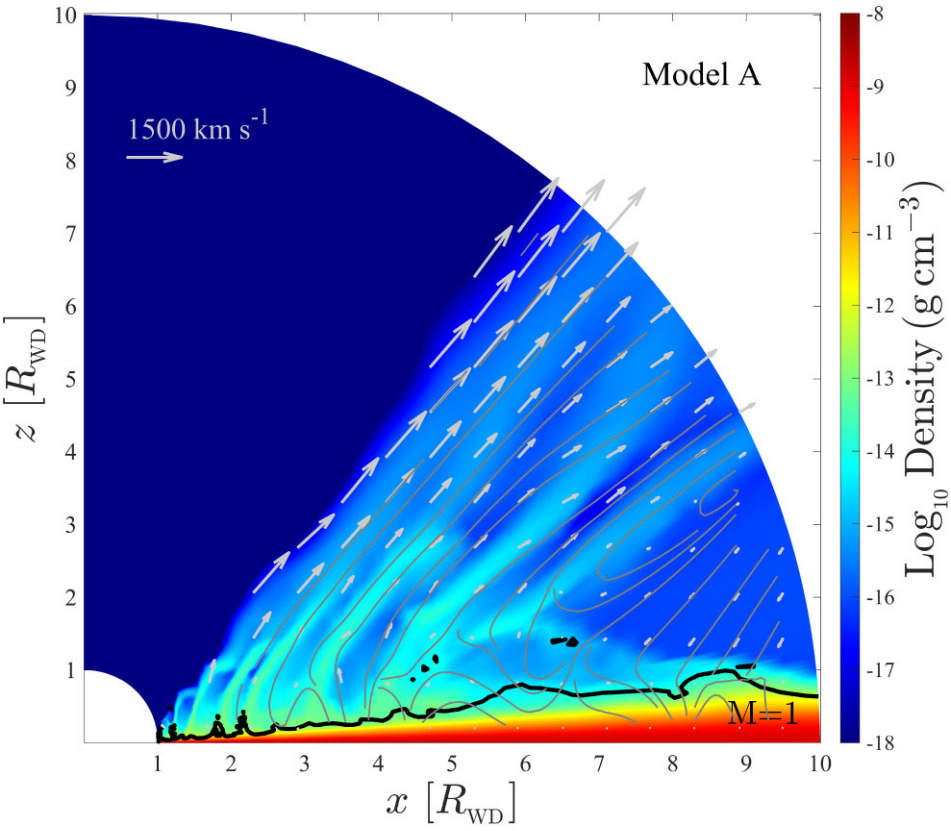

Figure 1. The density and poloidal velocity fields for the fiducial model at $t = 850$ s are shown. The colour map depicts the logarithmic density, while overlaid velocity vectors (normalized to a peak poloidal velocity of $v_{\rm p} = 1500\,{\rm km\,s^{-1}}$) illustrate the flow structure. Grey lines denote streamlines, and the solid black line marks the Mach 1 surface. For a version of the figure with logarithmically scaled x and z axes, see the top-right panel of Fig. 6. A line-driven disc wind is produced, with the bulk of the wind confined to a 25° wedge spanning polar angles from 40° to 65°.

vectors, normalized to a peak poloidal velocity of $v_{\rm p} = 1500\,{\rm km\,s^{-1}}$, illustrate the wind structure. Grey lines denote streamlines, and the solid black line marks the Mach 1 surface. A line-driven disc wind is produced, with the majority of the wind confined to a 25° wedge, spanning polar angles from 40° to 65°.

Fig. 2 displays snapshots of the density distribution for all four models at a similar time ($t = 850$ s, roughly one-fifth of the sound-crossing time-scale). All simulations have reached a quasi-steady state by this point (see Fig. 3 and discussion below). In each panel, we also show the corresponding poloidal velocity field, $v_{\rm p}$.

All four models produce similar line-driven disc winds, with comparable outflow geometries and velocity fields. In particular, the majority of the outflow is always confined to a 25° wedge spanning polar angles from 40° to 65°. The highly structured and variable nature of the outflow – a feature already noted in the earliest simulations by Proga et al. (1998) – is also consistent across all simulations.

Our new benchmark model, Model A, exhibits a slightly higher wind velocity compared to the other cases (cf. Table 1). Moreover, the inclusion of cooling and heating terms in the energy equation for the ideal runs (see the top- and bottom-left panels of Fig. 2) results in a narrower high-density region near the equatorial plane. As a consequence, the lower density environment in these models shifts the sonic (Mach 1) surface somewhat closer to the equator.

Perhaps the most important product of our simulations is the mass-loss rate through the outer radial boundary (i.e. $r_{\rm max}$). The total mass-outflow rate at this boundary is computed as

$$\dot{M}_{\rm wind} = 4\pi r_{\rm max}^2 \int_0^{85^\circ} \rho \max(v_{\rm r}, 0) \sin\theta \, {\rm d}\theta. \quad (22)$$

The upper limit of the integration here is set at 85° to exclude the dense and essentially hydrostatic disc atmosphere.

Fig. 3 illustrates the time evolution of the wind mass-loss rate ($\dot{M}_{\rm wind}$) for all four models. In all simulations, the mass-loss rate stabilizes to be approximately steady within 200 s. The remaining fluctuations in the mass-loss rates beyond this point are associated with the density structures apparent in Fig. 1, which remain time variable even in the quasi-steady state. The vertical dash–dotted line in Fig. 3 marks the timestamp corresponding to the representative snapshot shown in subsequent figures.

Fig. 3 shows that the mass-loss rates predicted by all simulations are broadly consistent, to within roughly the scatter expected from their intrinsic variability. More quantitatively, column (7) of Table 1 lists the time-averaged $\dot{M}_{\rm wind}$ over the interval $300 \leq t \leq 1500$ s. All four simulations produce values within roughly a factor of 2 of each other. This similarity in mass-loss rates demonstrates that the global properties of the wind are not particularly sensitive to the treatment of thermodynamics (isothermal versus full thermal balance) or to the details of the radiative transfer mode (classic versus hybrid macro-atom).

Crucially, the mass-loss rate in Model A remains a factor of 100 lower than the values found in previous simulations that did not treat the multidimensional radiative transfer and ionization in detail (e.g. Pereyra et al. 1997, 2000; Proga et al. 1998, 1999;

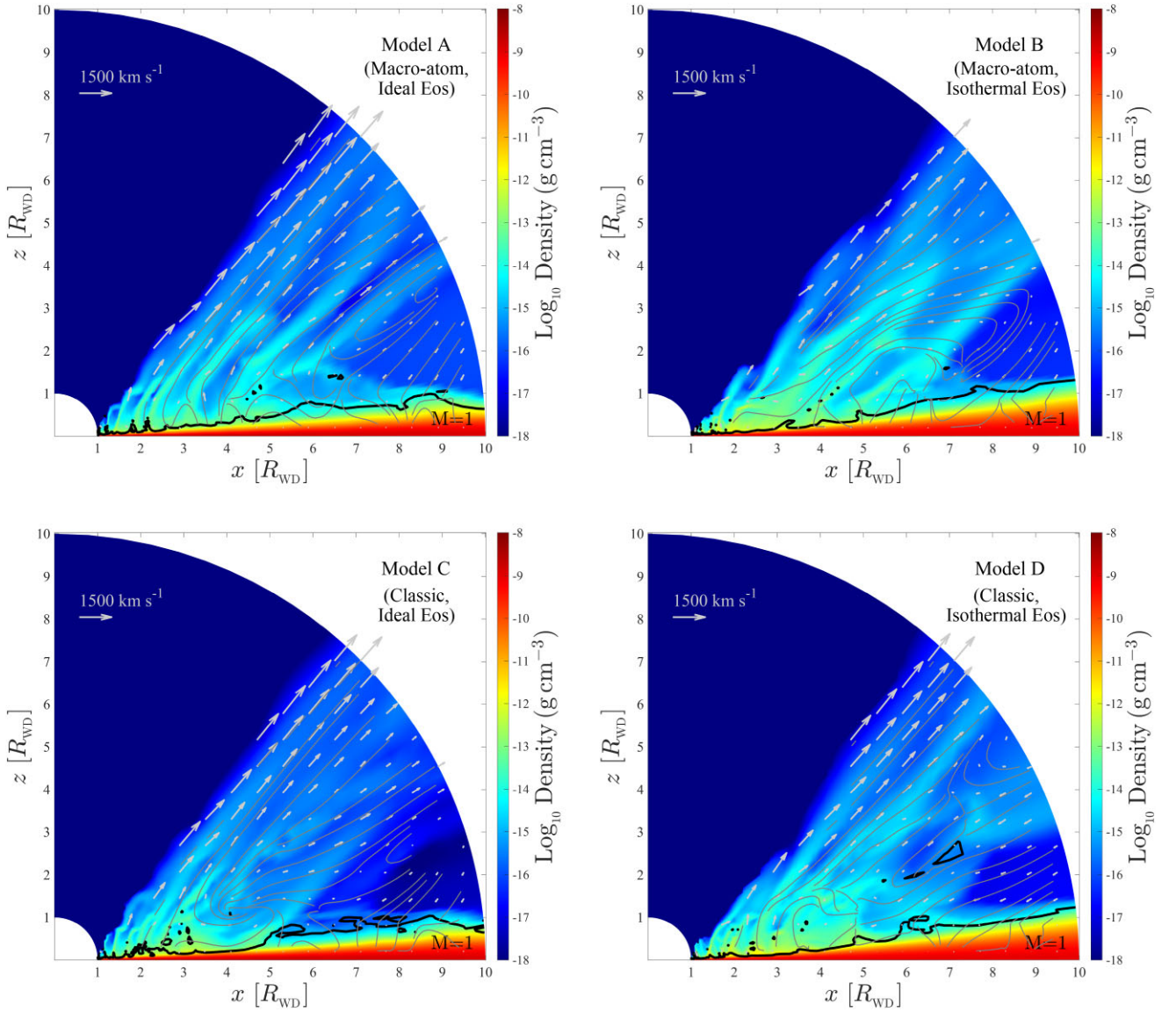

Figure 2. The density and poloidal velocity fields for Model A (top-left panel), Model B (top-right panel), Model C (bottom-left panel), and Model D (bottom-right panel; similar to Model HK22D of Higginbottom et al. 2024) at $t = 850$ s. The colour map represents the logarithmic density, while overlaid velocity vectors (normalized to a peak poloidal velocity of $v_{\rm p} = 1500\,{\rm km\,s^{-1}}$) illustrate the flow structure. Grey lines denote streamlines, and the solid black line marks the Mach 1 surface. Animated versions of each panel can be found in the supplementary material.

Dyda & Proga 2018a, b). Thus, the challenge to line driving highlighted by our previous work cannot be ascribed to the isothermal approximation adopted there, nor it is sensitive to the mode of radiative transfer used within SIROCCO. We will return to this issue in Section 4.

3.1 The wind temperature distribution

Fig. 4 displays the temperature structure of the outflow for Model A. Near the Mach 1 surface, where the wind is launched, we find $T \simeq 5 \times 10^4$ K. This is very similar to the value adopted in our isothermal models, $T = 4 \times 10^4$ K, which accounts for the good agreement between the models.

It is worth noting that there are some regions in the simulation – notably near the tips of the finger-like density structures – where advective heat transport becomes dominant over radiative or adiabatic heating/cooling. Strictly speaking, the assumption of instantaneous ionization equilibrium we make in SIROCCO also breaks down in these regions, since under these conditions the flow time-scale is likely to become shorter than the recombination time-scale. The ionization state would then become 'frozen-in' (see e.g. Drew & Verbunt 1985). However, this is unlikely to be a serious issue for the simulations here, since these regions are far from the wind-launching zone, and their temperature and ionization structure remain relatively constant (and physically reasonable) in any case.

3.2 Ionization state, force multipliers, and driving species

As previously discussed by Higginbottom et al. (2024), the relatively low mass-loss rates in our simulations are caused by the outflow becoming overionized. The actual outflows we observe in high-state AWDs do not seem to suffer from this problem. This discrepancy can be appreciated by comparing observed and predicted spectra. Fig. 5

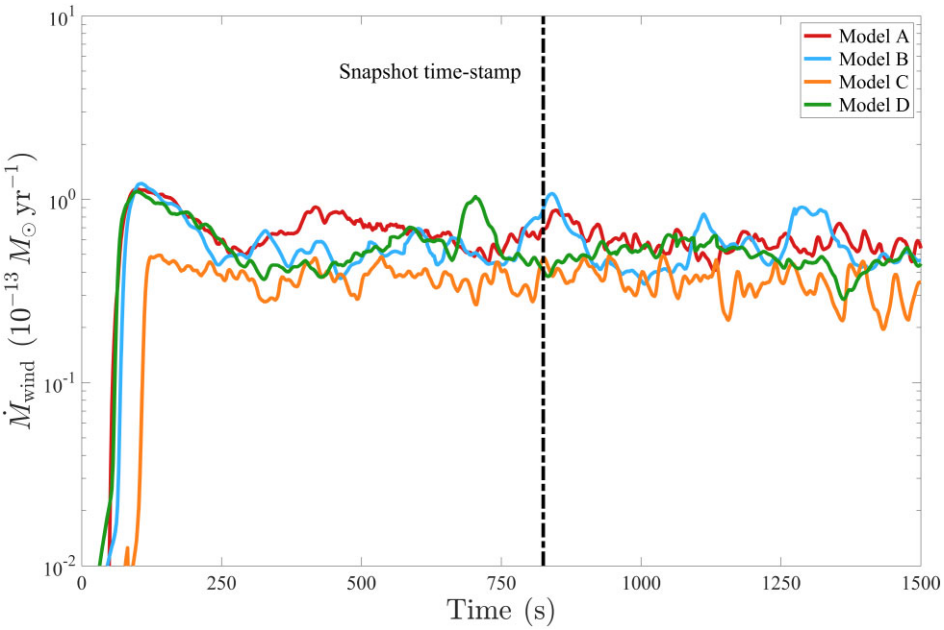

Figure 3. The time evolution of the wind mass-loss rate ($\dot{M}_{\rm wind}$) through the outer boundary for all four models. A vertical dash–dotted line marks the timestamp corresponding to the representative snapshot shown in subsequent figures. The high-density disc region is excluded in the calculation of $\dot{M}_{\rm wind}$.

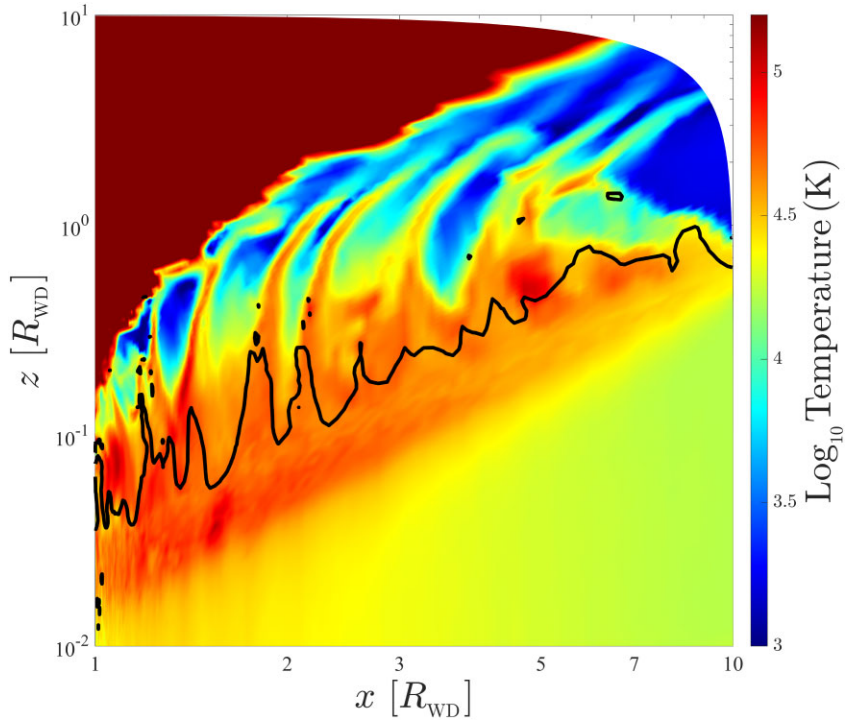

Figure 4. Two-dimensional temperature distribution from PLUTO hydrodynamic simulation snapshot of our fiducial model, shown on a logarithmic colour scale. The Mach 1 surface is indicated by the solid black line. Near this surface, temperatures reach a peak of $T \approx 5 \times 10^4$ K, in good agreement with the isothermal wind assumption of $T = 4 \times 10^4$ K used in isothermal models.

shows the UV spectra of two prototypical high-state AWDs (RW Sex, $i \simeq 30°$, and IX Vel, $i \simeq 65°$; *HST* program 14637 [PI: Long]). The dominant features here are strong, wind-formed resonance lines associated with N V 1240 Å, Si IV 1400 Å, and C IV 1550 Å. These features are weak or absent in the spectra predicted by SIROCCO for Model A for the same inclinations. This reflects the ionization state of the model wind, which favours higher ionization stages for each of these species.

In Fig. 6, we provide a more detailed picture of the ionization state of the wind and its impact on the force multiplier. In the top row of Fig. 6, we plot the distribution of density (left panel), force multiplier (middle panel), and oxygen ionization stages (right panel). In each

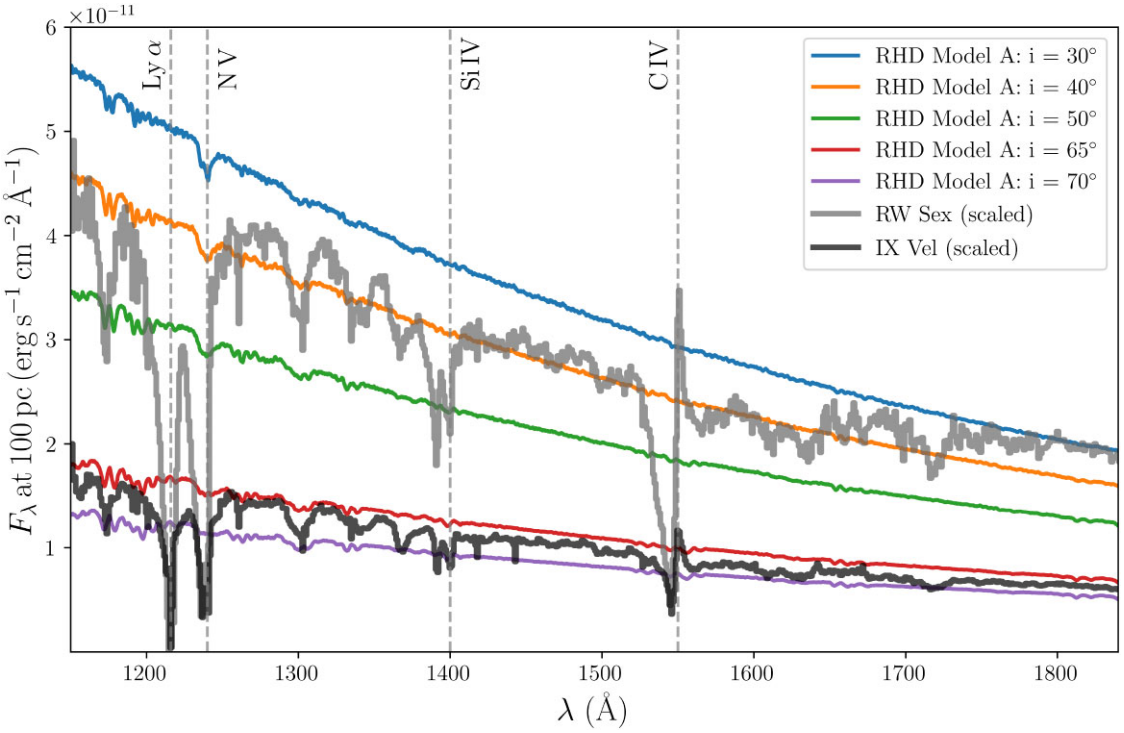

Figure 5. Synthetic UV spectra generated from a snapshot of the fiducial model for a range of inclination angles using SIROCCO. We also show the UV spectra of two prototypical high-state AWDs: RW Sex ($i \simeq 30°$) and IX Vel ($i \simeq 65°$). The spectra are normalized such that the flux levels correspond to a system observed at 100 pc. The positions of the Lyman limit and several key UV resonance lines are marked with vertical grey dashed lines.

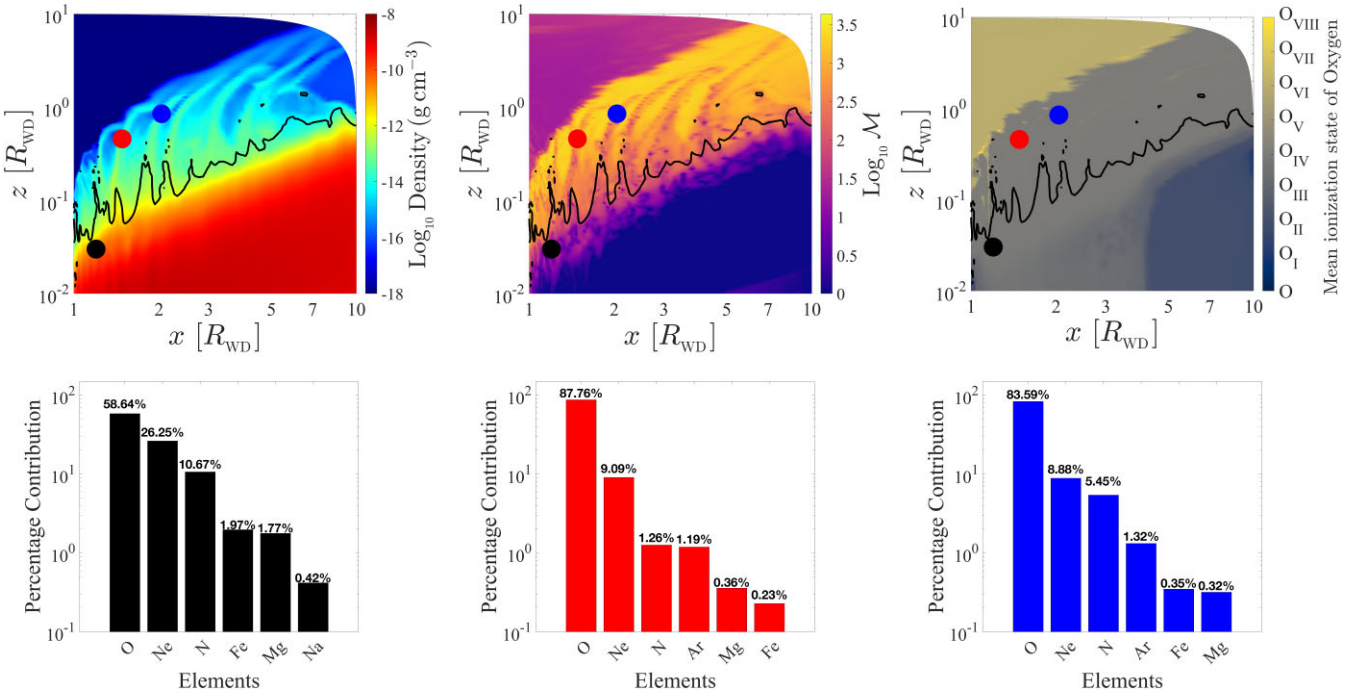

Figure 6. Top panels: Left panel displays the density map with logarithmic axes; middle panel presents the distribution of the force multiplier ($\mathcal{M}$); and right panel illustrates the mean ionization state of oxygen in our fiducial model. The solid black line marks the location of the Much 1 surface. Black, red, and blue dots indicate the positions of three representative cells selected for analysis in the simulation domain. Bottom panels: Percentage contributions of various elements to the total force multiplier at these representative points.

panel, three characteristic points in the outflow are marked, including one below the Mach 1 surface. In the bottom row, we additionally show a breakdown of the force multiplier by atomic species at each of these locations.

Fig. 6 illustrates two key points. First, the characteristic force multiplier in the wind-launching region (near the Mach 1 surface) is $\mathcal{M} \simeq$ a few $\times$ 100. This is (just) high enough for a line-driven wind to be produced in this simulation. However, it is far from the maximum force multiplier of $\mathcal{M} \simeq 4400$ expected for near-optimal conditions (e.g. Proga et al. 1998; Higginbottom et al. 2024), which could drive a strong wind in such a system.

Second, the dominant driving species in all three of our test locations is oxygen (mainly O IV), followed by neon and nickel. This is quite different from the powerful line-driven winds of hot stars, where transitions associated with iron tend to dominate the line force (e.g. Vink, de Koter & Lamers 1999; Noebauer & Sim 2015). This difference is a direct consequence of the different ionization states of – and characteristic optical depths in – these outflows. The relevant ionic species associated with Fe produce a huge number of weak lines, whereas those associated with O produce a smaller number of strong lines. High mass-loss rates tend to produce conditions in which strong lines are highly optically thick. Their contribution to the driving force then saturates, whereas that associated with weak lines can still grow in this regime. By contrast, the disc wind in our Model A is too weak to be optically thick even to strong lines. Since they are not saturated in this regime, they dominate the total driving force.

4 DISCUSSION

In Higginbottom et al. (2024), we presented the first RHD simulations of line-driven disc winds with a detailed multidimensional treatment of IRT. Our main result was that – at least in AWDs, but probably also in QSOs – it is much more difficult to generate the empirically inferred high mass-loss rates via this mechanism than expected previously. The fundamental reason is the susceptibility of line-driven winds to overionization: when exposed to a strong ionizing radiation field, the ionization state of the flow can easily tip into a regime in which bound–bound and bound–free opacities are too low for efficient line driving. The main remaining limitation of these simulations was that the outflow was assumed to be isothermal.

In the new simulations presented here, we have been able to relax this isothermal approximation, while also improving our treatment of IRT. We now explicitly and simultaneously solve for both ionization and thermal equilibrium throughout the flow. Despite these improvements, our results are very similar to those obtained in the isothermal approximation. Most importantly, overionization remains a problem, and the simulated outflows still produce much lower mass-loss rates ($\dot{M}_{\rm wind}/\dot{M}_{\rm acc} < 10^{-5}$, Table 1; also see Higginbottom et al. 2024) than earlier, more approximate simulations (which produced $\dot{M}_{\rm wind}/\dot{M}_{\rm acc} \simeq 10^{-4}$ for the same system parameters; see Proga et al. 1998, 1999). They also produce much weaker spectroscopic signatures than seen in observations.

Possible resolutions to this discrepancy between the predictions of line-driven disc wind theory and observations were discussed and explored by Higginbottom et al. (2024). For example, the overionization problem may be mitigated if the outflow is highly structured ('clumpy') on small, subgrid scales or if the irradiating SED is softer than that produced by a standard SSD. Additionally or alternatively, it is of course possible that mechanisms other than line driving – perhaps related to magnetic fields (e.g. Blandford & Payne 1982; Scepi et al. 2019) – may contribute to (or even dominate) the generation of these winds.

However, it is important to emphasize a critical point in this context. 'The observed spectra of high-state AWDs and BAL QSOs show unambiguously that the outflows in these systems do manage to avoid overionization'. As illustrated in Fig. 6 (for AWDs), they present precisely the strong UV resonance lines that are produced by the line-driven winds of hot stars. This suggests that line driving *can* be significant in these systems, even if other physical processes may also have to be involved in launching the observed outflows.

While there is much work left to be done to understand whether/how line driving works in AWDs, it is clearly also important now to investigate its relevance for AGN feedback. Line driving is commonly assumed to be the mechanism responsible for powering the outflows from these systems, but no hydrodynamic simulations with a multidimensional treatment of IRT have been carried out to date. In this context, our relaxation of the isothermal approximation is likely to be quite important, since the SEDs of AGN are more complex than those of high-state AWDs. It is difficult to predict the outcome of such simulations. On the one hand, AGN and QSOs can reach much higher Eddington ratios than AWDs, making it easier for radiative driving to work. On the other hand, overionization is also likely to be a significant challenge in these systems.

ACKNOWLEDGEMENTS

We would like to thank the referee for their insightful comments and constructive suggestions, which have helped to enhance the clarity and quality of this paper. AM and CK were supported by the UK's Science and Technology Facilities Council (STFC) grant ST/V001000/1. AW was supported by an STFC studentship grant 2750006. Partial support for KSL's effort on the project was provided by NASA through grant numbers HST-GO-16489 and HST-GO-16659 and from the Space Telescope Science Institute, which is operated by AURA, Inc., under NASA contract NAS 5-26555. SAS acknowledges funding from the STFC grant ST/X00094X/1. JHM acknowledges funding from a Royal Society University Research Fellowship (URF\R1\221062).

DATA AVAILABILITY

SIROCCO is freely available on GitHub, with documentation accessible via ReadTheDocs. The specific version of the combined PLUTO–SIROCCO code used in this work (PLUTO–SIROCCO v1.0) is archived on Zenodo (DOI:10.5281/zenodo.15792686) and can also be found at GitHub. The simulations were performed using a modified version of PLUTO v4.4 (Patch 3), coupled with the SIROCCO Monte Carlo radiative transfer code and an external CAK solver. Custom problem generators and input files are available from the authors upon request. Density movies of the simulation runs are provided as online supplementary material.

REFERENCES

Arav N., 1996, ApJ, 465, 617
Arav N., Korista K. T., Barlow T. A., Begelman, 1995, Nature, 376, 576
Blandford R. D., Payne D. G., 1982, MNRAS, 199, 883
Blondin J. M., 1994, ApJ, 435, 756
Castor J. I., Abbott D. C., Klein R. I., 1975, ApJ, 195, 157(CAK)
Castro Segura N. et al., 2022, Nature, 603, 52
Díaz Trigo M., Boirin L., 2016, Astron. Nachr., 337, 368
Drew J. E., Proga D., 2000, New Astron. Rev., 44, 21

Drew J., Verbunt F., 1985, MNRAS, 213, 191
Dyda S., Proga D., 2018a, MNRAS, 475, 3786
Dyda S., Proga D., 2018b, MNRAS, 478, 5006
Dyda S., Davis S. W., Proga D., 2024, MNRAS, 530, 5143
Dyda S., Dannen R. C., Kallman T. R., Davis S. W., Proga D., 2025, MNRAS, 540, 2612
Eddington A. S., 1916, MNRAS, 77, 16
Fabian A. C., 2012, ARA&A, 50, 455
Fabrika S., Ueda Y., Vinokurov A., Sholukhova O., Shidatsu M., 2015, Nat. Phys., 11, 551
Filbert S. et al., 2024, MNRAS, 532, 3669
Froning C. S., Long K. S., Gänsicke B., Szkody P., 2012, ApJS, 199, 7
Gayley K. G., 1995, ApJ, 454, 410
Gibson R. R. et al., 2009, ApJ, 692, 758
Harrison C. M., Costa T., Tadhunter C. N., Flütsch A., Kakkad D., Perna M., Vietri G., 2018, Nat. Astron., 2, 198
Higginbottom N., Proga D., 2015, ApJ, 807, 107
Higginbottom N., Knigge C., Long K. S., Sim S. A., Matthews J. H., 2013, MNRAS, 436, 1390
Higginbottom N., Proga D., Knigge C., Long K. S., Matthews J. H., Sim S. A., 2014, ApJ, 789, 19
Higginbottom N., Proga D., Knigge C., Long K. S., 2017, ApJ, 836, 42
Higginbottom N., Knigge C., Long K. S., Matthews J. H., Sim S. A., Hewitt H. A., 2018, MNRAS, 479, 3651
Higginbottom N., Knigge C., Long K. S., Matthews J. H., Parkinson E. J., 2019, MNRAS, 484, 4635
Higginbottom N., Scepi N., Knigge C., Long K. S., Matthews J. H., Sim S. A., 2024, MNRAS, 527, 9236
Howell S. B., Mason E., 2018, AJ, 156, 198
King A., 2003, ApJ, 596, L27
Korista K. T., Voit G. M., Morris S. L., Weymann R. J., 1993, ApJS, 88, 357
Liu C., Yuan F., Ostriker J. P., Gan Z., Yang X., 2013, MNRAS, 434, 1721
Long K. S., Knigge C., 2002, ApJ, 579, 725
Lu W.-J., Lin Y.-R., 2018, ApJ, 863, 186
Lucy L. B., 2002, A&A, 384, 725
Lucy L. B., 2003, A&A, 403, 261
Lucy L. B., Solomon P. M., 1970, ApJ, 159, 879
Mas-Ribas L., Mauland R., 2019, ApJ, 886, 151
Mata Sánchez D. et al., 2018, MNRAS, 481, 2646
Matthews J. H., Knigge C., Long K. S., Sim S. A., Higginbottom N., 2015, MNRAS, 450, 3331
Matthews J. H. et al., 2025, MNRAS, 536, 879
Middleton M. J., Walton D. J., Roberts T. P., Heil L., 2014, MNRAS, 438, L51
Middleton M. J., Higginbottom N., Knigge C., Khan N., Wiktorowicz G., 2022, MNRAS, 509, 1119
Mignone A., Bodo G., Massaglia S., Matsakos T., Tesileanu O., Zanni C., Ferrari A., 2007, ApJS, 170, 228
Miller J. M. et al., 2016, ApJ, 821, L9
Morganti R., 2017, Front. Astron. Space Sci., 4, 42
Mosallanezhad A., Yuan F., Ostriker J. P., Zeraatgari F. Z., Bu D.-F., 2019, MNRAS, 490, 2567
Mosallanezhad A., Bu D.-F., Čemeljić M., Zeraatgari F. Z., Hai Y., Mei L., 2022, ApJ, 939, 12
Muñoz-Darias T. et al., 2019, ApJ, 879, L4
Noebauer U. M., Sim S. A., 2015, MNRAS, 453, 3120
Nomura M., Ohsuga K., 2017, MNRAS, 465, 2873
Nomura M., Ohsuga K., Takahashi H. R., Wada K., Yoshida T., 2016, PASJ, 68, 16
Nomura M., Ohsuga K., Done C., 2020, MNRAS, 494, 3616
Parkin E. R., Sim S. A., 2013, ApJ, 767, 114
Pereyra N. A., Kallman T. R., Blondin J. M., 1997, ApJ, 477, 368
Pereyra N. A., Kallman T. R., Blondin J. M., 2000, ApJ, 532, 563
Ponti G., Fender R. P., Begelman M. C., Dunn R. J. H., Neilsen J., Coriat M., 2012, MNRAS, 422, L11
Proga D., 2003, ApJ, 592, L9
Proga D., Kallman T. R., 2004, ApJ, 616, 688
Proga D., Stone J. M., Drew J. E., 1998, MNRAS, 295, 595
Proga D., Stone J. M., Drew J. E., 1999, MNRAS, 310, 476
Proga D., Stone J. M., Kallman T. R., 2000, ApJ, 543, 686
Proga D., Kallman T. R., Drew J. E., Hartley L. E., 2002, ApJ, 572, 382
Scepi N., Dubus G., Lesur G., 2019, A&A, 626, A116
Shakura N. I., Sunyaev R. A., 1973, A&A, 24, 337
Silk J., Rees M. J., 1998, A&A, 331, L1
Sim S. A., Drew J. E., Long K. S., 2005, MNRAS, 363, 615
Sim S. A., Proga D., Miller L., Long K. S., Turner T. J., 2010, MNRAS, 408, 1396
Stevens I. R., Kallman T. R., 1990, ApJ, 365, 321
Tetarenko B. E., Lasota J. P., Heinke C. O., Dubus G., Sivakoff G. R., 2018, Nature, 554, 69
Tomaru R., Done C., Ohsuga K., Odaka H., Takahashi T., 2020, MNRAS, 497, 4970
Vink J. S., de Koter A., Lamers H. J. G. L. M., 1999, A&A, 350, 181

SUPPORTING INFORMATION

Supplementary data are available at *MNRAS* online.

suppl_data

Please note: Oxford University Press is not responsible for the content or functionality of any supporting materials supplied by the authors. Any queries (other than missing material) should be directed to the corresponding author for the article.

This paper has been typeset from a TEX/LATEX file prepared by the author.